

Facile fabrication of hierarchical PVDF/Mg-Al LDH/chitosan membrane for textile wastewater remediation: role of LDH in anchoring chitosan

Downloaded from: https://research.chalmers.se, 2025-11-29 20:30 UTC

Citation for the original published paper (version of record):

Xue, Y., Shao, J., Lê, X. et al (2026). Facile fabrication of hierarchical PVDF/Mg-Al LDH/chitosan membrane for textile wastewater

remediation: role of LDH in anchoring chitosan. Journal of Membrane Science, 739. http://dx.doi.org/10.1016/j.memsci.2025.124914

N.B. When citing this work, cite the original published paper.

research.chalmers.se offers the possibility of retrieving research publications produced at Chalmers University of Technology. It covers all kind of research output: articles, dissertations, conference papers, reports etc. since 2004. research.chalmers.se is administrated and maintained by Chalmers Library

ELSEVIER

Contents lists available at ScienceDirect

Journal of Membrane Science

journal homepage: www.elsevier.com/locate/memsci



Facile fabrication of hierarchical PVDF/Mg–Al LDH/chitosan membrane for textile wastewater remediation: role of LDH in anchoring chitosan

Yongtao Xue, Jieling Shao D, Huy Xuan Le, Jia Wei Chew D

Department of Chemistry and Chemical Engineering, Chalmers University of Technology, Gothenburg, 412 96, Sweden

ARTICLE INFO

Keywords:
Layered double hydroxides
Chitosan
Hierarchical membrane
Textile wastewater
Structural bridging role

ABSTRACT

Layered double hydroxides (LDHs), as two-dimensional nanomaterials with abundant hydroxyl groups and unique layered structures, have been shown to be promising candidates to improve membrane properties for enhancing textile wastewater remediation. In this study, a PVDF/Mg-Al LDH membrane was prepared through a non-solvent-induced phase separation method, and then the hierarchical PVDF/Mg-Al LDH/chitosan membrane was fabricated through a facile filtration process. The resulting optimized membrane demonstrated an acceptable water permeance (2.3 L m⁻² h⁻¹ bar⁻¹) and excellent separation efficiency for mixtures of dye and salt (i.e., rejections of 99.9 % for Congo red, 100 % for Methyl blue, and <20 % for NaCl). Notably, the separation factor of the PVDF/Mg-Al LDH/chitosan membrane for Congo red/NaCl reached up to 1934, surpassing most membranes reported in the literature. In addition, the hybrid membrane demonstrated outstanding antifouling performance (flux recovery ratio of 92.68 % for Methyl blue and 90.31 % for Congo red), and high stability under acidic and alkaline conditions. Characterization results and mechanism analysis indicate that the Mg-Al LDH nanoparticles not only improved the membrane's hydrophilicity and modulated its structure, but also played a structural bridging role within the membrane to anchor chitosan through hydrogen bonding. Mechanistic studies confirm that the size-sieving and Donnan effects were responsible for the separation of dyes and salts. This study unveils the structural bridging role of Mg-Al LDH within the membrane and provides new insights into the facile fabrication of hybrid membranes for efficient textile wastewater remediation.

1. Introduction

Water pollution constitutes a significant impediment to sustainable development, with effluents from the textile industry representing a particularly acute concern, contributing approximately 20 % of the total global wastewater discharge [1,2]. In general, textile wastewater contains various hazardous and nonbiodegradable organic dyes, as well as relatively high concentrations of salts (e.g., NaCl), and directly releasing textile wastewater into the environment can result in severe ecological, environmental, and public health ramifications [3,4]. Therefore, efficient removal of dyes and salt recovery is urgently needed to achieve sustainable water recycling and resource circularity. To address this, membrane-filtration has been recognized as promising, mainly due to its inherent advantages including high selectivity and removal efficiency, environmental friendliness, relatively low energy consumption, and scalability [5–7].

Polyvinylidene difluoride (PVDF) is one of the most popular and commonly used materials for the fabrication of membranes due to its outstanding thermal and chemical stability, and superior mechanical properties [8]. However, PVDF are hydrophobic, leading to issues like poor water flux and increased fouling, restricting their wider application [9]. To enhance the hydrophilicity of PVDF membranes, various modification strategies have been investigated [10-13]. Among these, the incorporation of hydrophilic nanoparticles into the membrane matrix to fabricate hybrid membranes has emerged as particularly promising, as it not only improves hydrophilicity but also optimizes membrane porosity and surface characteristics, thereby enhancing overall performance. Notably, layered double hydroxides (LDH), which are composed of positively charged metal cation layers and negatively charged intercalated anion layers, have attracted considerable attention owing to their unique two-dimensional layered structure and tunable properties [14]. In addition, Mg-Al LDH is a relatively low-cost and environmentally friendly nanomaterial with abundant hydroxyl groups. In this study, the hypothesis is that the appropriate amount of Mg-Al LDH nanoparticles can improve hydrophilicity, increase the active sites, and adjust the pore structure of the membrane, enhancing the separation efficiency of dyes

E-mail address: jia.chew@chalmers.se (J.W. Chew).

^{*} Corresponding author.

and salts.

On the one hand, the intercalated anions of Mg-Al LDH are easily replaced by anionic dyes through anion exchange, resulting in excellent adsorption capacity for anionic dyes [15]. Moreover, the high adsorption capacity causes serious membrane fouling, which reduces the lifetime of the membrane and limits practical application. To balance the trade-off, optimization of Mg-Al LDH concentration and coating an effective separation layer on the membrane surface are efficient methods to simultaneously prevent membrane fouling and increase separation efficiency. Among the coating materials used for membrane modification, chitosan is popular due to it being a natural and green polymer with abundant amino and hydroxyl groups, along with its low cost and hydrophilicity [16]. As shown in Table S1, the coating of chitosan onto the membrane surface has mainly been achieved through cross-linking, polymerization, or electrospinning methods, which are complicated processes that require multiple chemicals or expensive equipment, and thus are difficult to scale up. To leverage the benefits, a scalable and facile method for the fabrication of PVDF/Mg-Al LDH/chitosan hybrid membranes is highly desired. Considering that both Mg-Al LDH and chitosan contain abundant hydroxyl groups, it appears a feasible strategy to immobilize chitosan onto the Mg-Al LDH membrane through hydrogen bonding effects. For instance, Lin et al. [17] confirmed that the hydrophilic covalent organic frameworks with abundant N, O electron donors and -OH groups could interact with -OH and -NH2 groups of chitosan through hydrogen bonding for the fabrication of dense and stable composite membrane. Li et al. [18] also observed that the strong hydrogen bonding effects between MXene and tannic-3-aminopropyltriethoxysilane promoted the structural stability of the obtained membrane. However, as summarized in Table S2, previous studies on LDH-based membranes primarily utilized its hydrophilicity, surface charge, and layered structure to enhance membrane water permeance and anti-fouling performance for wastewater treatment. Hydrogen bonding between LDH -OH groups and chitosan -OH/-NH2 groups during the hybrid-membrane preparation has not been examined. In such hybrid membranes, LDH not only increases the hydrophilicity and regulates the structure of the membrane, but also plays a structural bridging role for the immobilization of chitosan. Hence, this study targeted deciphering the structural bridging role of LDH in the facile fabrication of hierarchical PVDF/Mg-Al LDH/chitosan membranes.

In this study, the optimized amount of Mg-Al LDH nanoparticles was integrated into the casting solution for the fabrication of the Mg-Al LDH membrane through a non-solvent-induced phase separation method. Subsequently, the chitosan layers were immobilized onto the Mg-Al LDH membrane through a facile filtration process for the construction of the hierarchical PVDF/Mg-Al LDH/chitosan membrane. The prepared membranes were systematically characterized in terms of porosity, pore size, thickness, morphology, chemical structure, and surface property. The separation efficiency of dyes/salts, antifouling performance, thermal stability, and longer-term stability of the PVDF/Mg-Al LDH/chitosan membranes were also investigated. Additionally, the separation mechanisms for dyes/salts and the structural bridging role of LDH within the PVDF/Mg-Al LDH/chitosan membrane were comprehensively discussed. The results are expected to provide an innovative and facile strategy for the fabrication of hierarchical membranes for efficient textile wastewater remediation.

2. Materials and methods

2.1. Preparation of Mg-Al LDH and membranes

All the chemicals were used directly without any further purification, and ultrapure water was used throughout the experiment. Detailed chemical descriptions are provided in Text S1 of the Supplementary Information. The Mg–Al LDH nanomaterials were synthesized according to the reported method [19]. In brief, 5.12~g of Mg(NO₃)₂·6H₂O and

3.75~g of Al(NO₃) $_3\cdot 9H_2O$ were dissolved in 100 mL water, and then 6 g of urea were added. The mixture was continuously stirred for 10 min at room temperature to obtain a homogenous solution (total volume around 110 mL, pH around 3). Subsequently, the solution was transferred into a Teflon-lined autoclave (200 mL) and heated at 110 $^{\circ}\text{C}$ for 24 h. The resulting products were washed with water through centrifugation at 4000 rpm and dried at 80 $^{\circ}\text{C}$ overnight. The yield of Mg–Al LDH nanomaterials was approximately 83 %, and the detailed calculation method is provided in Texts S2 of the Supplementary Information.

The PVDF/Mg–Al LDH membrane was fabricated through a non-solvent-induced phase separation method. Specifically, 16 wt% of PVDF and 2 wt% of polyethylene glycol (PEG) were dispersed into the 1-Methyl-2-pyrrolidone (NMP) solution (82 wt%), and then 0.25 wt% of Mg–Al LDH was added, after which the mixture was ultrasonicated for 5 min. Subsequently, the mixture was heated at 50 $^{\circ}\text{C}$ for 6 h under continuously stirring conditions for the formation of a homogeneous casting solution. Finally, this solution was cast on a clean glass plate to a thickness of 200 μm (casting solution thickness) through a film applicator, and then the glass plate was immediately immersed in a water bath at room temperature for phase inversion. The pure PVDF membrane was also prepared using the same method without the addition of Mg–Al LDH.

The PVDF/Mg-Al LDH-chitosan membrane was also prepared through a facile filtration process (Fig. 1). First, 0.01 g of chitosan was completely dissolved in 100 mL acetic acid solution (2 wt%) and kept at continuously stirring conditions for 12 h to form a uniform solution. Next, 6 mL of chitosan solution was loaded on the surface of the PVDF/ Mg-Al LDH membrane via dead-end filtration (Sterlitech HP4750 cell) at 4 bar for 30 min to result in the PVDF/Mg-Al LDH-chitosan membrane. The concentrations of chitosan were selected to represent a typical range relevant to membrane surface modification. Based on preliminary experiments, four composite membranes were prepared using various chitosan concentrations - 0.01 wt% (0.041 mg/cm²), 0.03 wt% (0.123 mg/cm²), 0.05 wt% (0.205 mg/cm²), 1 wt% (0.411 mg/ cm²)) - designated as LDH-CS-1, LDH-CS-3, LDH-CS-5, and LDH-CS-10, respectively. The applied chitosan concentrations ranged from relatively low (0.01 wt%) to high (1 wt%) levels, enabling a comprehensive evaluation of the influence of chitosan content on composite membrane performance. All the chitosan were completely dissolved under the experimental conditions; therefore, the potential effect of chitosan solubility at different pH levels on membrane uniformity was not considered during the filtration and deposition processes. All membranes used in the experiments were freshly fabricated, with a storage period not exceeding 24 h prior to testing. Separation performance measurements were conducted in triplicate, and the standard errors of the means are presented in the corresponding figures.

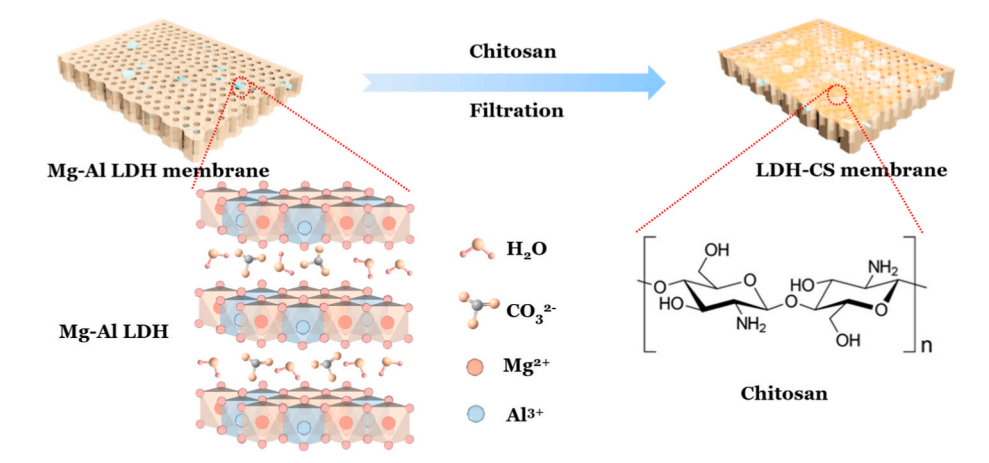
2.2. Characterization and measurements

The characterization, and separation and antifouling performance of the prepared membranes are detailed in Texts S3–S5 of the Supplementary Information.

3. Results and discussion

3.1. Structures and properties of Mg-Al LDH nanoparticles

The crystal structure and elemental composition of the prepared Mg–Al LDH were characterized by XRD. As illustrated in Fig. 2a, the characteristic diffraction peaks at $2\theta=11.5^\circ, 23.3^\circ, 34.7^\circ, 39.3^\circ, 47.0^\circ, 53.3^\circ, 56.7^\circ, 60.8^\circ, 62.1^\circ,$ and 66.2° correspond respectively to the (003), (006), (012), (015), (018), (1010), (0111), (110), (113), and (116) planes typical of Mg–Al LDH (JCPDS. 35–0964) [20]. The basal spacing (d) of 0.769 nm was observed for Mg–Al LDH from the (003) plane ($2\theta=11.5^\circ$), indicating the successful integration of CO_3^{2-} anions in the layer [21]. The parameter a=2 d (110) is related to the average



 $\textbf{Fig. 1.} \ \ \textbf{Schematic diagram depicting the fabrication of the Mg-Al LDH-chitosan membrane.}$

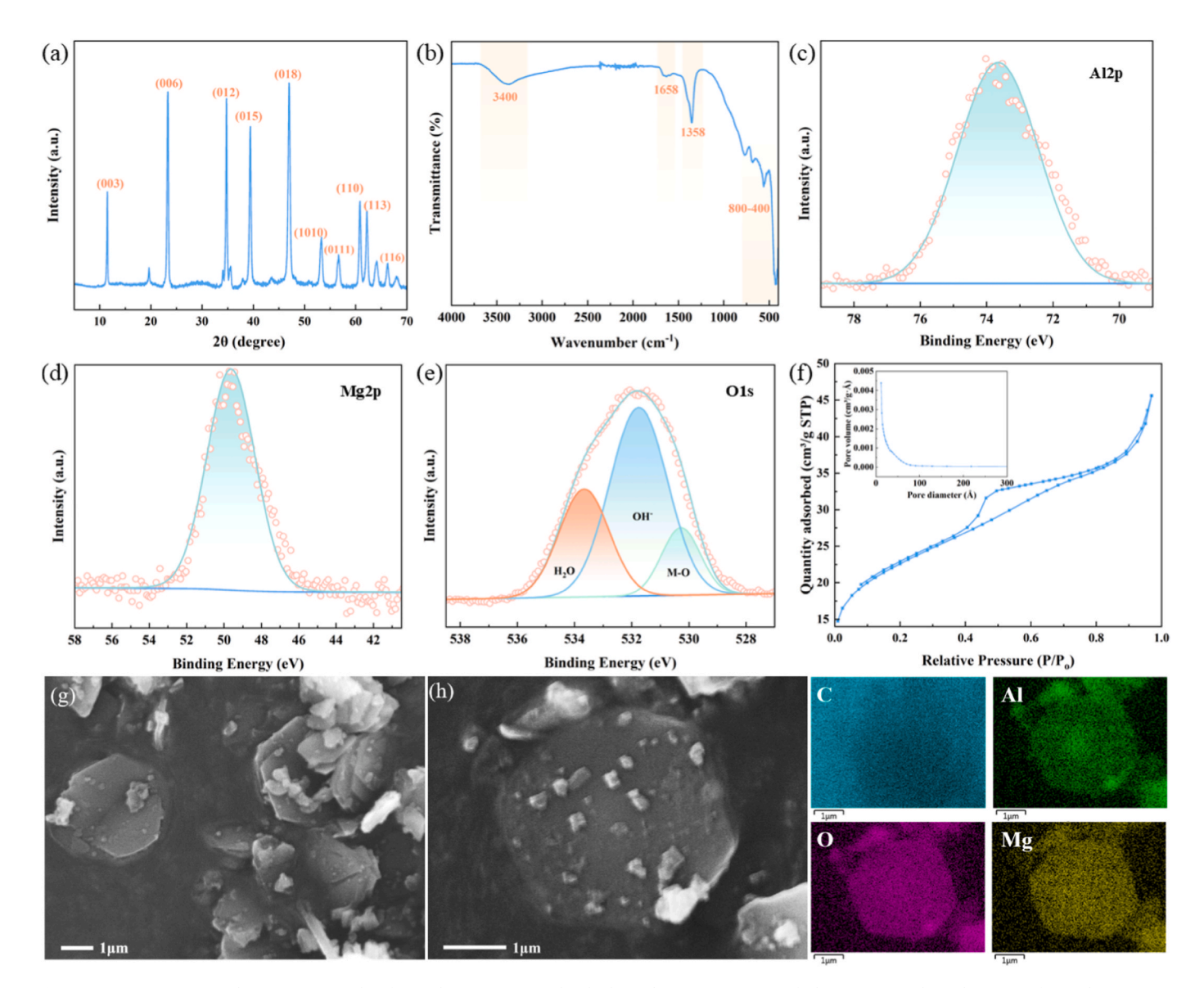


Fig. 2. XRD patterns (a) and FTIR spectrum (b) of Mg-Al LDH nanoparticles, high-resolution XPS spectra of Al2p (c), Mg2p(d), and O1s (e) of Mg-Al LDH nanoparticles, N_2 adsorption and desorption isotherms and pore size distribution of Mg-Al LDH nanoparticles (f), SEM image (g) and elemental mapping images (h) of Mg-Al LDH nanoparticles.

distance of cation-cation in the layer, and another parameter c = 3d(003) represents the electrostatic interaction between the layer and the interlayer [22]. Hence, the average distance of cation-cation (a) and the electrostatic interaction in layers (c) for the prepared Mg-Al LDH were calculated as 3.04 Å and 23.1 Å, respectively. In addition, the average crystal size of Mg-Al LDH was determined to be 26 nm. All the above results confirm the successful preparation of Mg-Al LDH nanomaterials, whose molecular formula has been identified as Mg₄Al₂(OH)₁₂CO₃·nH₂O. In addition, the functional groups of Mg-Al LDH were also identified through FTIR. In Fig. 2b, the broad peak is at approximately 3400 cm⁻¹, corresponding to the stretching vibrations of O-H and water molecules in the interlayer of Mg-Al LDH [23]. The peak around 1658 cm⁻¹ is ascribed to H–O–H bending vibrations of interlayer water [24]. The peak at 1358 cm⁻¹ is related to the CO₃²⁻ groups, confirming that CO_3^{2-} as interlayer anions were intercalated into Mg-Al LDH [19]. Additionally, peaks between 800 and 400 cm⁻¹ are attributed to the vibrations of Al-O and Mg-O [25]. These observed peaks reveal the prepared Mg-Al LDH has a layered structure.

The chemical composition and valence state of Mg-Al LDH was explored by XPS. In Fig. S1a, the survey spectrum displays the characteristic peaks of C1s, O1s, Mg 2p, and Al 2p, confirming the presence of these elements in the Mg-Al LDH. In Fig. 2c-d, the characteristic peaks at 73.7 eV and 49.6 eV are ascribed to the Al 2p and Mg 2p within the Mg-Al LDH, respectively [26]. The C1s spectrum (Fig. S1b) shows three characteristic peaks at 284.8 eV, 287.1 eV, and 290.0 eV, which are attributed to the C-C band, C-O band, and CO_3^{2-} , respectively [27]. The O1s spectrum (Fig. 2e) also displays three peaks around 530.2 eV, 531.7 eV, and 533.6 eV, which are assigned to the lattice oxygen, hydroxide ionized oxygen, and adsorbed water, respectively [28]. These XPS results further confirm the layered structure of Mg-Al LDH. Additionally, the specific surface area and pore structures of Mg-Al LDH were evaluated through N2 adsorption and desorption isotherm. As illustrated in Fig. 2f, the prepared Mg-Al LDH exhibits a typical Type IV isotherm with an H₃ type hysteresis loop at P/P₀ of 0.4-0.8, indicating the presence of mesoporous structures [29]. The specific surface area and average pore size of Mg–Al LDH were calculated to be 81.71 m^2/g and 2.81 nm, respectively. Moreover, the morphologies of Mg–Al LDH nanoparticles were investigated through SEM analysis. Fig. 2g shows that the Mg–Al LDH nanoparticles exhibited a hexagonal sheet structure with a certain degree of agglomeration, and the size of the hexagonal sheet was around 2 μm . The elemental mapping (Fig. 2h) confirms the C, O, Mg, and Al elements were uniformly distributed, indicating the successful preparation of Mg–Al LDH nanoparticles.

3.2. Characterization of the prepared membranes

The surface functional groups of fabricated membranes were investigated through FTIR analysis. As illustrated in Fig. S2a, the pure PVDF powder displays three different crystalline phases including α phase, β phase, and γ phase. Specifically, the peaks at 839 cm⁻¹ and 1278 cm⁻¹ are related to the β phase [30], while the peaks at 762 cm⁻¹ and 433 cm⁻¹ are attributed to the α phase and γ phase, respectively [31]. The bending vibration of CH₂ was also observed at 1401 cm⁻¹ and 873 cm⁻¹ [32]. The stretching vibration of C-F was found at 1173 cm⁻¹ and 1069 cm⁻¹, and the peak of 486 cm⁻¹ is associated with the bending vibrations of C-F [32]. For PEG (Fig. S2b), the peaks at 3468 cm⁻¹, 1278 cm⁻¹, and 1242 cm⁻¹ are due to the stretching vibration of O–H bands, and the strong peak at 1100 cm⁻¹ indicates the stretching vibration of C-O [33]. The peaks at 2886 cm⁻¹, 1446 cm⁻¹, 1342 cm⁻¹, 960 cm⁻¹, and 842 cm⁻¹ are related to the vibrations of C-H [34]. In Fig. S2c, the broad peak at 3350 cm⁻¹ in chitosan is ascribed to the stretching vibrations of O-H and N-H [35]. The peaks at 1654 cm⁻¹ and 1582 cm⁻¹ represent the C=O vibrations of the amide I band and protonated amine II band, respectively [36]. The vibrations of C-H are tied to the peaks of 2877 cm⁻¹, 1417 cm⁻¹, and 1378 cm⁻¹, while the stretching vibration of C-O was also observed at the peak of 1024 cm⁻¹ [37]. As shown in Fig. 3a, the main peak positions in the FTIR spectrum of the PVDF membrane closely resemble those of the PVDF powder. Specifically,

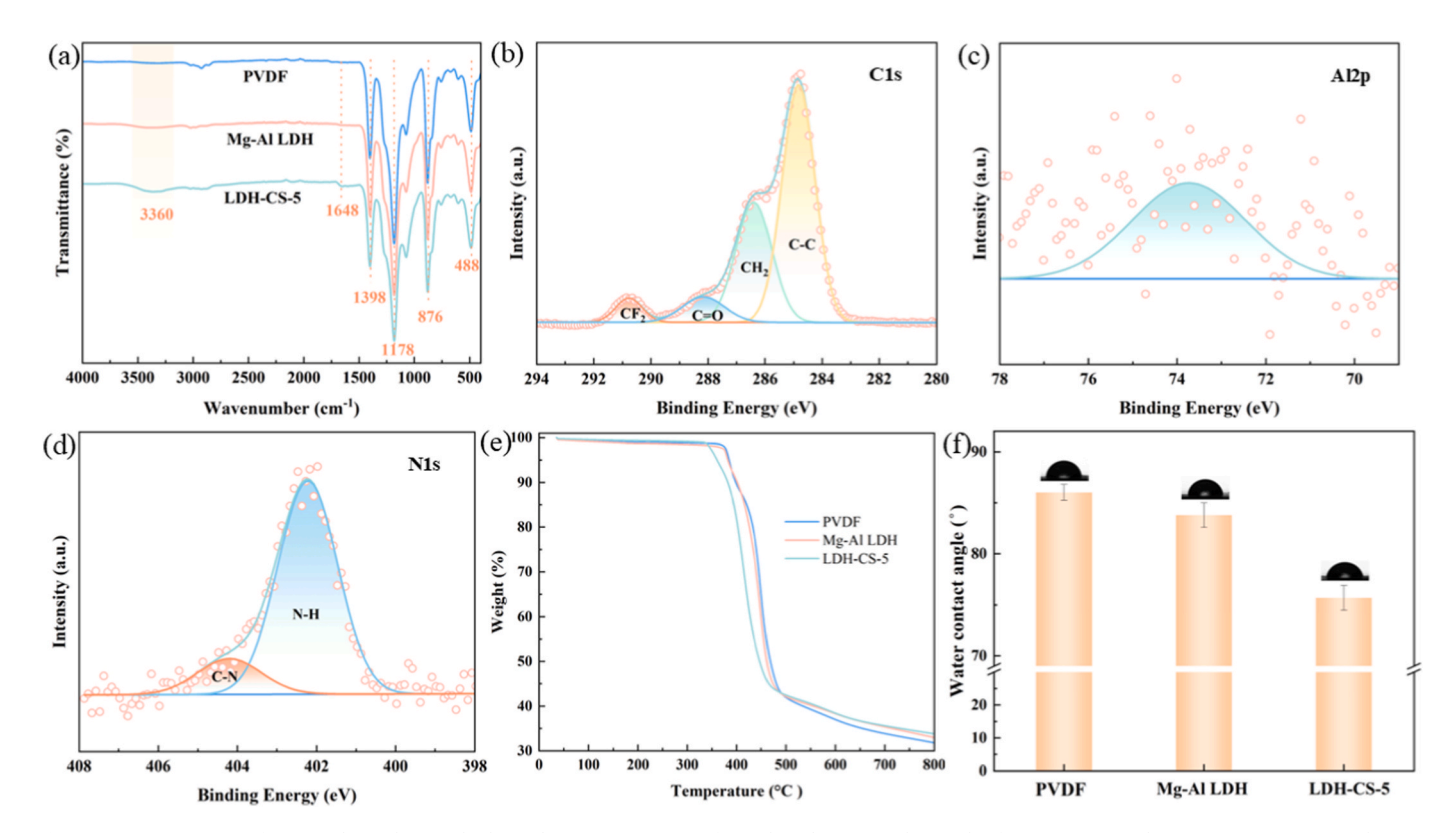


Fig. 3. FTIR spectra (a) of prepared membranes, high-resolution XPS spectra of C1s (b), Al2p (c), and N1s (d) of LDH-CS-5 membrane, TGA curves (e) and water contact angle (f) of prepared membranes.

characteristic peaks of PVDF were observed at 1398 cm $^{-1}$, 1178 cm $^{-1}$, 876 cm $^{-1}$, and 488 cm $^{-1}$ in the membrane spectrum. In addition, no obvious peaks of PEG were found, revealing that PEG mainly contributed to pore formation in the membrane structure [38]. A broad peak at 3360 cm $^{-1}$ is related to the O–H band in the Mg–Al LDH membrane, indicating that Mg–Al LDH was successfully integrated into the membrane matrix. In addition, two peaks at 3360 cm $^{-1}$ and 1648 cm $^{-1}$ in the LDH–CS–5 are ascribed to the characteristic peaks of chitosan, confirming the successful fabrication of the PVDF/Mg–Al LDH/chitosan membrane.

The surface chemical properties of prepared membranes were also explored through XPS analysis. In Fig. S3a, the survey spectrum of the PVDF membrane displays the characteristic peaks of C1s, O1s, and F1s. The C1s spectrum (Fig. S3b) is divided into four peaks at around 284.8 eV, 286.2 eV, 287.8 eV, and 290.6 eV, which are attributed to the C-C, CH₂, C=O, and CF₂ bands, respectively [39]. In addition, the O1s (Fig. S3c) and F1s (Fig. S3d) spectra also confirm the presence of C=O and CF₂ bands, respectively. These results prove the main composition of PVDF membrane was PVDF. After the addition of Mg-Al LDH (Fig. S4a), there were no obvious changes for C1s (Fig. S4b) and F1s (Fig. S4e) between the PVDF membrane and PVDF/Mg-Al LDH membrane. In Fig. S4c, three peaks at 530.0 eV, 531.5 eV, and 532.6 eV in O1s of the PVDF/Mg-Al LDH membrane are attributed to the lattice oxygen, C=O, and adsorbed water, respectively. Fig. S4d exhibits the characteristic peak of Al2p with relatively low intensity, suggesting that the Mg-Al LDH nanoparticles were successfully integrated into the PVDF/Mg-Al LDH membrane matrix. Meanwhile, the main structure of the PVDF membrane did not significantly change after the addition of Mg-Al LDH nanoparticles due to the low concentration of Mg-Al LDH nanoparticles. For the LDH-CS-5 membrane (Fig. S5), the relative intensities of CF2 in the C1s (Fig. 3b) and Al2p (Fig. 3c) spectra markedly decreased, which are primarily due to the chitosan surface coating partially masking the characteristic peaks of PVDF and Mg-Al LDH. The N1s spectrum of LDH-CS-5 membrane (Fig. 3d) shows two peaks at 402.2 eV and 404.1 eV, corresponding to N-H and C-N, respectively [40]. In Fig. S5b, four peaks located at 530.6 eV, 532.0 eV, 533.0 eV, and 534.0 eV are in accordance with lattice oxygen, C=O, O-H, and adsorbed water, respectively [41]. The presence of abundant O-H and N-H bands confirms the successful incorporation of chitosan into the LDH-CS-5 membrane. In addition, the C=O binding energy shifts from 531.5~eV to 532.0~eV in the PVDF/Mg–Al LDH membrane relative to the LDH-CS-5 membrane, indicating the formation of hydrogen bonds between LDH and chitosan. The upshift arises because interaction with electrophilic N-H/O-H protons decreases electron density of C=O, increasing its binding energy [17]. It should be also noted that the positions of O-H and N-H bands in the LDH-CS-5 membrane are slightly higher compared to the existing literature, which may be related to the formation of hydrogen bonds between chitosan and LDH [42].

The thermal stability of the prepared membranes was evaluated through TGA analysis. In Fig. S6, the PVDF powder exhibits a remarkable weight loss after 400 °C, which is related to the decomposition of C-H and C-F bands [43]. For Mg-Al LDH powder, the rapid weight loss from 30 $^{\circ}\text{C}$ to 250 $^{\circ}\text{C}$ is attributed to removing the absorbed water and interlayer water, while the sustained weight loss from 250 $^{\circ}\text{C}$ to 500 $^{\circ}\text{C}$ is associated with decarbonization and dihydroxylation of Mg-Al LDH [44]. Two major weight losses of chitosan were also observed at 30°C-150 °C and 150°C-400 °C, corresponding to the loss of adsorbed water and decomposition of organic functional groups, respectively [45]. As illustrated in Fig. 3e, all the prepared membranes demonstrate similar TGA curves as with PVDF powder, implying that the main composition of fabricated membranes was PVDF. The TGA curve of the Mg-Al LDH membrane was slightly shifted to lower temperatures compared to the PVDF membrane, revealing that the concentration of Mg-Al LDH nanoparticles was relatively low in the PVDF/Mg-Al LDH membrane. Although the LDH-CS-5 membrane exhibited the lowest decomposition temperature of 340 $^{\circ}$ C (370 $^{\circ}$ C for PVDF and Mg–Al LDH

membranes) among all the prepared membranes, the thermal stability is still excellent since it remains stable below 300 $^{\circ}\text{C}.$

In addition, the surface hydrophilicity of membranes was also studied through the water contact angle analysis. In Fig. 3f, the LDH-CS-5 membrane gave the lowest water contact angle (75.6°) compared with the PVDF membrane (86.0°) and PVDF/Mg-Al LDH membrane (83.7°), indicating that the LDH-CS-5 membrane had the highest surface hydrophilicity among all the prepared membranes. The enhanced surface hydrophilicity of the LDH-CS-5 membrane is attributed to the integration of abundant surface hydrophilic functional groups (e.g., O-H) of Mg-Al LDH and chitosan into the membrane matrix. Notably, the surface hydrophilicity not only facilitates the transport of water molecules through the membrane, but also improves the membrane's fouling resistance through the formation of a water layer on the membrane surface [46]. The porosity and pore size are two key parameters that can significantly affect the membrane performance. Fig. S7 shows that the mean pore radius of the PVDF/Mg-Al LDH membrane slightly decreased compared to the PVDF membrane, indicating that the embedding of Mg-Al LDH nanoparticles into the membrane structures reduced the membrane pore size. The porosity and pore size of the LDH-CS-5 membrane were further reduced, revealing that chitosan partially obstructed the pores of the PVDF/Mg-Al LDH membrane. The specific surface area and pore size distribution of the LDH-CS-5 membrane were also measured through N2 adsorption and desorption isotherms. In Fig. S8, the specific surface area and average pore size of LDH-CS-5 membrane were determined to be $10.8 \text{ m}^2/\text{g}$ and 4.85 nm, respectively, confirming the coexistence of micropores and mesopores in the membrane structure. In Fig. S9, the thicknesses of the as-prepared PVDF, Mg-Al LDH, and LDH-CS-5 membranes were measured using a micrometer as 110.5 μm , 111.2 μm , and 113.8 μm , respectively. Although Mg-Al LDH nanoparticles influence the phase separation rate during membrane fabrication, their relatively low loading in the casting solution had a negligible effect on membrane thickness and instead primarily modified the internal structure (e.g., pore size). Therefore, PVDF membrane and Mg-Al LDH membrane have similar thicknesses. As for the effect of chitosan on the membrane thickness, per the chitosan coating amount (0.205 mg/cm²) and density (1 g/cm³), the thickness of the chitosan layer deposited on the membrane surface would be $2.05 \mu m$. That the LDH-CS-5 membrane was approximately $2 \mu m$ thicker is consistent with the deposition of chitosan on the surface.

The surface and cross-sectional morphologies of the prepared membranes are presented in Fig. 4. The PVDF membrane exhibited a flat surface with abundant nanopores (Fig. 4a), and the cross-sectional image shows the PVDF membrane had asymmetric structures and relatively high porosity (Fig. 4d). The incorporation of Mg-Al LDH nanoparticles into the membrane matrix significantly changed the morphologies of the PVDF/Mg-Al LDH membrane. Fig. 4b and e show that the PVDF/Mg-Al LDH membrane exhibited mesh-like surfaces with some nanoparticles and sponge-like internal structures, and the pores of the membrane were also significantly reduced. The elemental mapping images (Fig. S10) of the PVDF/Mg-Al LDH membrane prove that the C, F, O, Mg, and Al elements were homogeneously distributed into the membrane matrix, suggesting that the Mg-Al LDH nanoparticles were successfully embedded into the membrane. As a hydrophilic nanomaterial, the integration of Mg-Al LDH nanoparticles into a casting solution can accelerate the exchange rate between water and organic solution (NMP) and further increase the phase separation rate. In this case, the enlargement of pores was inhibited due to the fast phase separation rate and confinement effects, resulting in more small pores being generated within the membrane [47]. It should be also noted that the incorporation of nanoparticles into the casting solution normally increases the viscosity of the solution, which can reduce the phase separation rate [48]. However, the hydrophilic effects of Mg-Al LDH nanoparticles in the casting solution were predominant due to their relatively low concentration in this study. In Fig. 4c and f, the LDH-CS-5

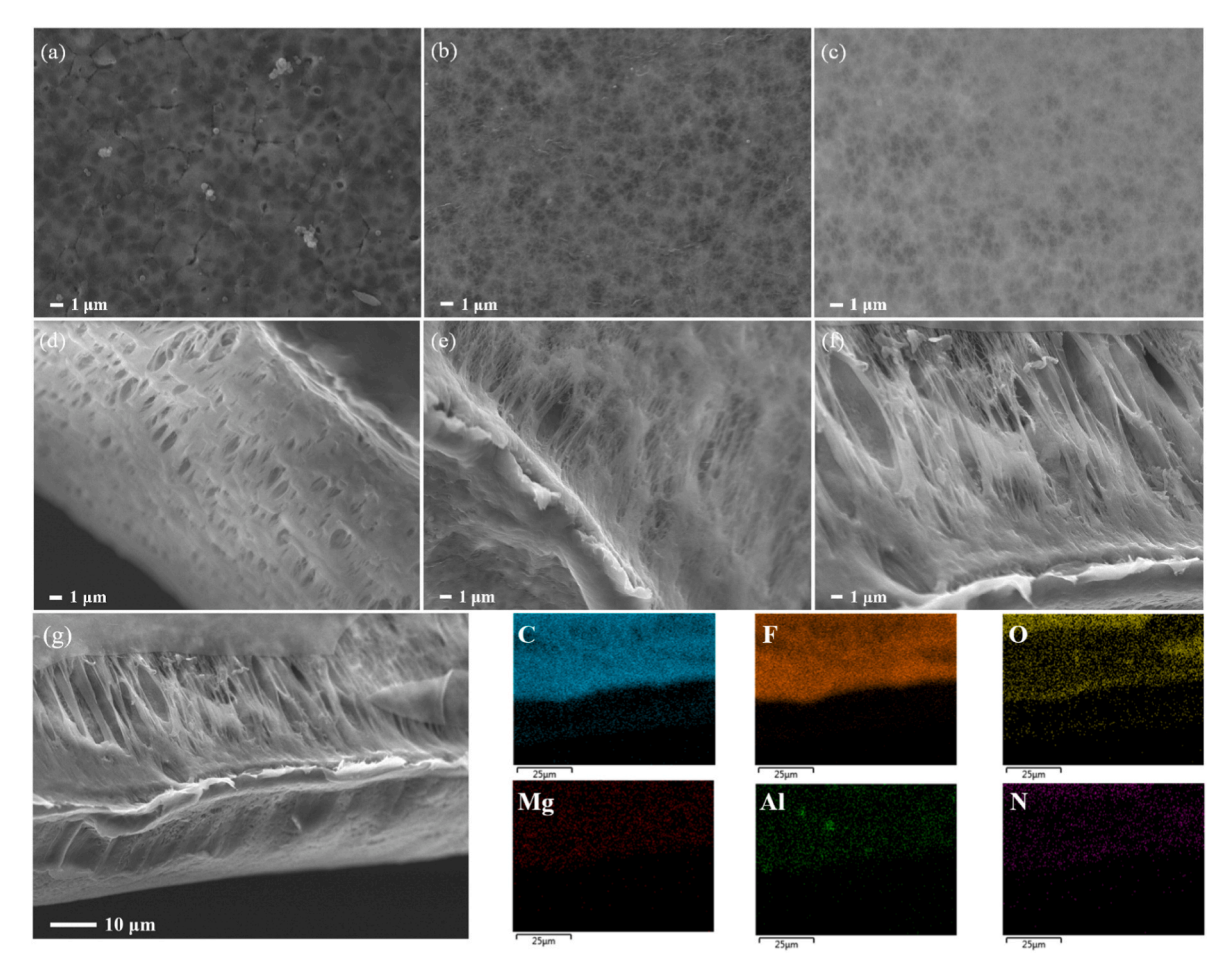


Fig. 4. Top-view and cross-sectional SEM images of PVDF membrane (a, d), PVDF/Mg–Al LDH membrane (b, e), and LDH–CS–5 membrane (c, f), and elemental mapping images (g) of LDH–CS–5 membrane (cross-section).

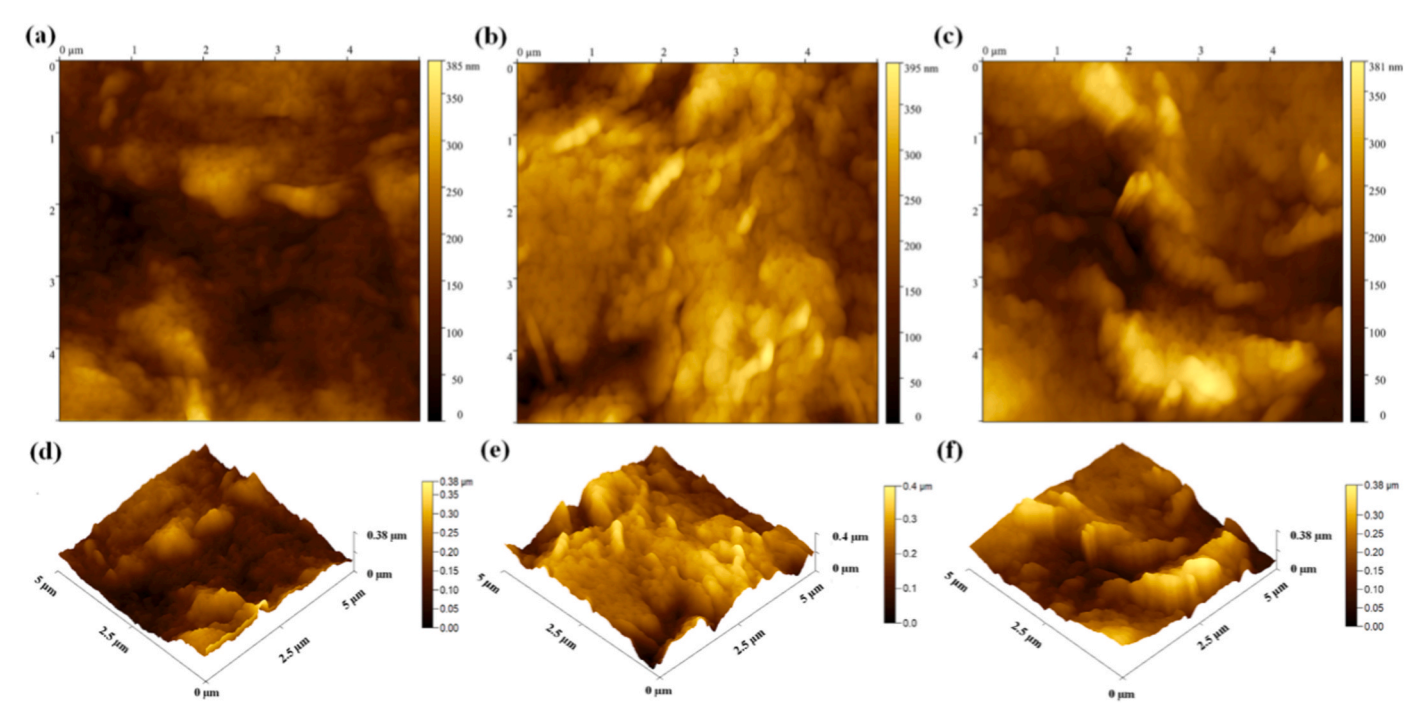


Fig. 5. 2D and 3D AFM images of PVDF membrane (a, d), PVDF/Mg-Al LDH membrane (b, e), and LDH-CS-5 membrane (c, f).

membrane displays similar surface morphologies to the PVDF/Mg-Al LDH membrane, while the morphologies of the cross-section are slightly changed, which is related to the integration of chitosan into the membrane structure. Fig. 4g shows the C, F, O, Mg, Al, and N elements were uniformly dispersed in the membrane matrix, indicating that chitosan was not only on the membrane surface but also dispersed in the internal structures of the membrane. In addition, the EDX line scan results of the top view (Fig. S11a-c) of the LDH-CS-5 membrane demonstrate that C and F are the main elements on the membrane surface, while the contents of Mg, Al, and N are relatively low. EDX line scanning results of the membrane cross-section (Fig. S11d-f) also indicate trace amounts of Mg, Al, and N elements, revealing that the Mg-Al LDH and chitosan were integrated into the membrane structure, which is consistent with the results of elemental mapping. According to the results, it can be concluded that Mg-Al LDH nanoparticles were uniformly distributed into the PVDF membrane matrix, while most of the chitosan molecules were deposited on the membrane surface. Therefore, the Mg-Al LDH/PVDF membrane primarily served as the support layer in the LDH-CS-5 membrane, while chitosan functioned as the surface separation layer.

Furthermore, the surface roughness of the prepared membranes was determined through arithmetic mean roughness (Ra) and root mean square roughness (Rq). As illustrated in Fig. 5 and Fig. S12, all the fabricated membranes exhibited wrinkled and valley-like structures. The PVDF/Mg–Al LDH membrane (Ra = 41.5 nm) had a rougher surface than the PVDF membrane (Ra = 37.8 nm). This phenomenon can be explained by two main mechanisms. Firstly, part of the Mg–Al LDH nanoparticles migrated to the membrane surface during the membrane formation process, thereby increasing the membrane surface roughness [49]. Secondly, the accelerated separation rate during the phase inversion process induced one-dimensional shrinkage of surface polymer chains in a non-solvent environment, resulting in the formation of spheres or nodules of polymer, which further augmented the surface roughness [50]. The LDH–CS–5 membrane had the highest surface

roughness value (Ra = 45.5 nm) among all the prepared membranes, which is related to the agglomeration of chitosan molecules on the membrane surface. Past studies have demonstrated that rougher membrane surfaces can provide more effective surface areas, allowing for higher water permeance [51]. Nonetheless, the relatively rough membrane surface is associated with higher fouling tendencies, since pollutants are easily deposited in the valleys of the roughness elements [52]. In this study, the surface roughness of the LDH–CS–5 membrane slightly increased from 37.8 nm to 45.5 nm compared to the PVDF membrane, balancing the trade-off between increased water permeance and increased fouling, as demonstrated in the following section.

3.3. Separation performance for dyes and salt

The pure water permeance of the prepared membranes was assessed. As shown in Fig. 6a, the pure water permeance slightly decreased from 23.1 L m⁻² h⁻¹ bar⁻¹ to 18.6 L m⁻² h⁻¹ bar⁻¹ after the addition of Mg-Al LDH nanoparticles. This is mainly due to the reduced pore size and increased thickness of the PVDF/Mg-Al LDH membrane, resulting in the increased resistance to water permeating through the membrane. The pure water permeance of LDH-CS membranes also gradually decreased with the increase of chitosan concentrations. This phenomenon is ascribed to the relatively high chitosan concentration, which not only blocked the pores of the membrane but also formed a dense surface chitosan layer, resulting in higher resistance to permeation. These results were further confirmed through the investigation of dye rejection efficiency. In Fig. 6b-c, all the prepared membranes exhibited similar relative water permeance values in the presence of either MB or CR, but the water permeance of were lower compared to Fig. 6a. In addition, the PVDF/Mg-Al LDH membrane demonstrated higher rejections for MB (94.5 %) and CR (97 %) compared to the PVDF membrane (90.6 % and 95.5 %, respectively). The LDH-CS membranes displayed excellent rejection efficiency for MB and CR, with LDH-CS-5 achieving complete rejection of MB and CR. Lower concentrations of chitosan were

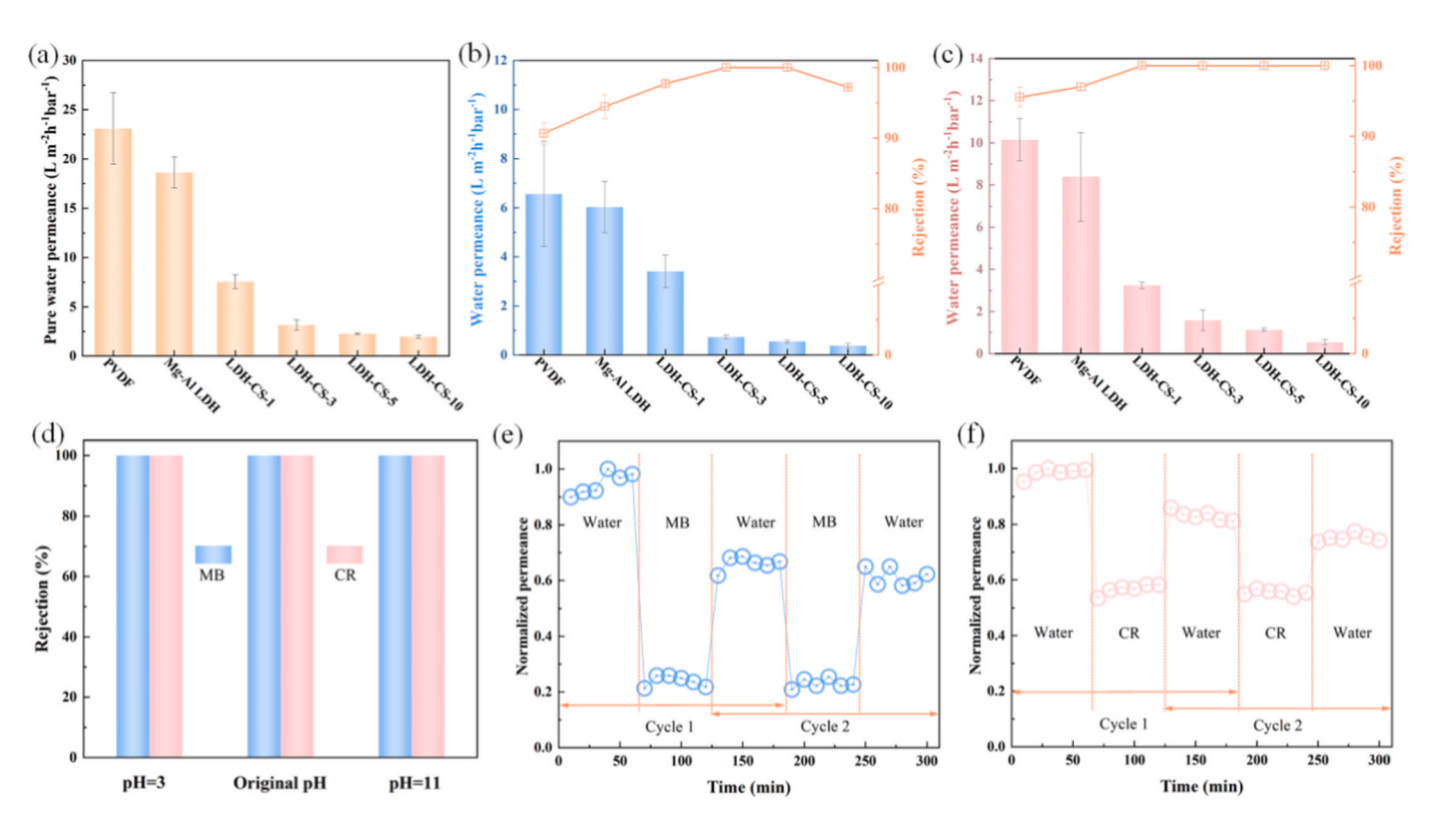


Fig. 6. Pure water permeance (a) and separation performance for (b) MB and CR (c) by prepared membranes, separation efficiency for MB and CR under different pH values by LDH-CS-5 (d), antifouling performance over 2 cycles of LDH-CS-5 for MB (e) and CR (f).

insufficient to reduce the pore size and change the surface properties of the membrane, leading to relatively low rejection efficiency for MB and CR. The chemical stability of the LDH–CS–5 membrane was also examined through the separation of MB and CR under pH values ranging from 3 to 11. Fig. 6d shows complete rejections of MB and CR by the LDH–CS–5 membrane. The chemical stability of the prepared membrane was also evaluated using FTIR spectroscopy. As shown in Fig. S13, the membranes subjected to acid and alkali treatments exhibited spectra similar to those of the untreated samples, with no significant changes in characteristic absorption peaks, indicating excellent chemical stability.

Moreover, since membrane fouling is a serious problem that can significantly reduce the service life of membranes in real applications, practical membranes need to be equipped with excellent antifouling ability. The antifouling performance of the prepared membranes was investigated by using MB and CR as the target pollutants. As illustrated in Fig. 6e–f, the water permeance dramatically decreased upon the introduction of MB or CR to the feed, which is due to membrane fouling. After the used membrane was cleaned by pure water, water permeance recovered to different degrees. In Fig. S14, four parameters including flux recovery ratio (FRR), total fouling ratio ($R_{\rm t}$), reversible fouling ratio

 $(R_{\rm r})$, and irreversible fouling ratio $(R_{\rm ir})$ were applied to evaluate the antifouling performance of the membrane. Notably, the LDH–CS–5 membrane exhibited high FRR (92.68 % for MB and 90.31 % for CR) and low $R_{\rm ir}$ (7.32 % for MB and 9.69 % for CR) in the second cycle. To further simulate real wastewater conditions, antifouling experiments were performed using a mixture of CR and NaCl. As shown in Fig. S15, the LDH–CS–5 membrane exhibited a high FRR of 93 % during the second filtration cycle with the CR-NaCl mixture, indicating excellent antifouling performance. This is primarily ascribed to the enhanced surface hydrophilicity of the membrane promoting the formation of a hydration layer that alleviates the adhesion of dyes onto the membrane surface [53].

Generally, textile wastewater contains high concentrations of salts and dyes. Therefore, dye and salt mixtures were employed to assess the separation efficiency of the LDH-CS-5 membrane. As depicted in Fig. 7a, the LDH-CS-5 membrane exhibited excellent dye rejection (>99 %) and relatively low salt rejection efficiency (<20 %), and the separation factor for CR was calculated to be 1934. These results affirm that the LDH-CS-5 membrane is promising for the separation of dye and salt mixtures. Additionally, the comparation between the prepared

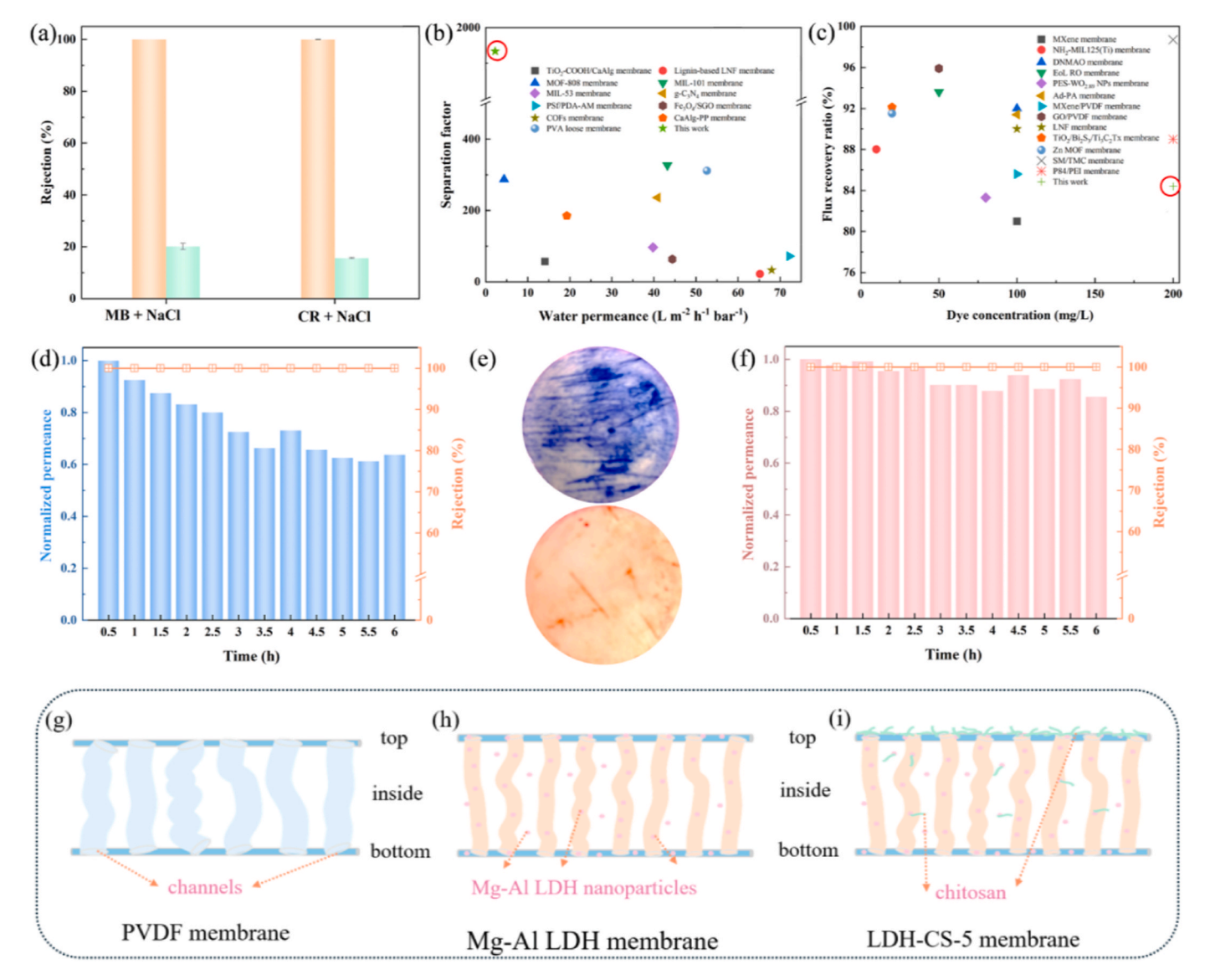


Fig. 7. Separation performance of LDH-CS-5 membrane for dye/salt mixture solution (a), the performance comparison of LDH-CS-5 membrane with previously reported membranes (b-c), long-term stability of LDH-CS-5 membrane for the separation of MB (d) and CR (f), digital photo of the used membrane (e), schematic diagram of the prepared membranes (g-i).

LDH–CS–5 membrane and reported membranes in the literature were summarized in Tables S4–S5 and Fig. 7b–c. As shown in Fig. 7b, although the water permeance of the prepared LDH–CS–5 membrane is relatively lower compared to earlier studies, its separation factor is exceptionally high, exceeding that of most membranes reported. In this study, the formation of a dense chitosan layer on the surface of the LDH–CS–5 membrane imparts greater permeation resistance while enhancing dye rejection efficiency, thereby yielding favorable separation factors despite reduced water permeance. This observation underscores the intrinsic trade-off between selectivity and permeability. Future research should focus on optimizing the membrane pore structure and hydrophilicity to improve water permeance without compromising selectivity. Fig. 7c indicates that the LDH–CS–5 membrane offers advantages in terms of reasonable antifouling performance at high dye concentrations.

Additionally, the long-term stability of the LDH-CS-5 membrane was assessed for the separation of MB and CR. Fig. 7d and f show that the LDH-CS-5 membrane displayed excellent rejection efficiency (near 100 %) for MB and CR over 6 h, while the water permeance decreased more in the case of MB than CR. The decreased water permeance can be ascribed to two phenomena. Firstly, the chitosan layer on the surface was further compacted over time during the pressure-driven filtration, resulting in higher resistance to permeation. Secondly, the hydrophilic dye molecules have high affinity to the hydrophilic Mg-Al LDH and chitosan, increasing the fouling tendency. Nevertheless, the prepared membrane exhibited good antifouling properties, and thus the dye molecules on the membrane surface can be easily removed. As can be seen in Fig. 7e, the used membranes were only slightly colored after the 6 h experiments, indicating that the membrane had good stability and antifouling properties. In addition, the LDH-CS-5 membrane maintained 100 % removal efficiency for both MB and CR, as well as over 80 % of its initial water permeance after five filtration cycles (Fig. S16). The excellent retention of separation performance demonstrates the LDH-CS-5 membrane's durability and indicates its potential suitability for long-term operations and application in real textile wastewater treatment.

3.4. Mechanism analysis

Based on the results, the mechanism analysis is presented in Fig. 7g-i. The PVDF membrane (Fig. 7g) had large pore sizes and low hydrophilicity, resulting in relatively high water permeance and low rejection of dyes. With the uniform embedding of Mg-Al LDH nanoparticles, Fig. 7h illustrates that pore sizes were reduced, and hydrophilicity and surface roughness of the PVDF/Mg-Al LDH membrane were increased. In the LDH-CS-5 membrane, most of the chitosan were deposited onto the membrane surface, while only a small fraction penetrating into the interior. In this configuration, Mg-Al LDH nanoparticles not only enhanced the membrane's hydrophilicity and modulated its structure, but also served as molecular bridges that anchor the chitosan molecules via hydrogen bonds (Fig. 7i), resulting in chitosan being stably immobilized in the PVDF/Mg-Al LDH membrane matrix. Evidence for hydrogen bonding is supported by FTIR and XPS analyses; while this interpretation is widely accepted, more direct confirmation (e.g., neutron diffraction) would be valuable in future studies. Incorporation of chitosan further reduced pore size, increased membrane thickness, and enhanced hydrophilicity and surface roughness. In general, the dye separation mechanisms by membranes can be largely classified into size sieving, Donnan effect, and surface adsorption [54]. In this study, the LDH-CS-5 membrane had a relatively low specific surface area of $10.8\,\text{m}^2/\text{g}$, and the slight coloring of the membranes after 6 h of filtration suggests adsorption was not the dominant mechanism, due to chitosan alleviating the fouling extent. In the dye/salt mixture, the dispersion of dyes is improved due to the combination of high salt concentration and anionic dye [55], leading to the rejection efficiency of CR being slightly decreased. In addition, the low rejection of salt is ascribed to the molecular size of NaCl being much smaller than MB/CR, causing the size-sieving effect to be significantly reduced. Chitosan is generally regarded as positively charged due to the presence of abundant NH₂ groups on its surface [56]. Additionally, the Donnan effect underlying electrostatic repulsion between the positively charged Na⁺ and positively charged chitosan on the membrane surface led to the improvement of salt rejection efficiency [57]. Therefore, the LDH–CS–5 membrane demonstrated excellent separation factors for dye and salt mixtures. These results suggest that the size sieving effect and the Donnan effect governed the rejection of dyes, while the Donnan effect was the dominant mechanism for the rejection of salt. Moreover, the developed pore structures and hydrophilic surface of the membrane also promoted the transport of water molecules. In summary, the LDH–CS–5 membrane, with excellent separation efficiency for dye/salt mixtures, is promising for real textile wastewater remediation.

4. Conclusions

In this study, the hierarchical PVDF/Mg-Al LDH/chitosan membrane was innovatively and systematically fabricated by utilizing the structural bridging effect of Mg-Al LDH to immobilize chitosan. The characterization results demonstrate that the Mg-Al LDH nanoparticles were uniformly distributed into the PVDF membrane matrix, while most of the chitosan were deposited on the membrane surface. The resulting PVDF/Mg-Al LDH/chitosan membrane exhibited smaller pore sizes, increased thickness, higher hydrophilicity and higher surface roughness compared to pristine PVDF membrane, leading to excellent separation efficiency for dye and salt mixtures (namely, 99.9 % for Congo red, 100 % for Methyl blue, and <20 % for NaCl). In addition, the optimized membrane exhibited a superior separation factor of 1934 for Congo red/ NaCl mixture, with size-sieving and Donnan effects identified as the dominant separation mechanisms. Moreover, the membrane also demonstrated excellent antifouling performance (flux recovery ratios of 92.68 % for Methyl blue and 90.31 % for Congo red) and high stability in both acidic and alkaline media. This study provides a comprehensive evaluation of the respective roles of Mg-Al LDH and chitosan within the composite membrane, while also presenting a proof-of-concept strategy for the facile fabrication of hierarchical membranes. While the results are promising, they remain preliminary, and further systematic validation is necessary before potential industrial implementation can be realized.

CRediT authorship contribution statement

Yongtao Xue: Writing – review & editing, Writing – original draft, Visualization, Validation, Methodology, Investigation, Formal analysis, Data curation, Conceptualization. Jieling Shao: Investigation. Huy Xuan Le: Investigation. Jia Wei Chew: Writing – review & editing, Validation, Supervision, Resources, Project administration, Funding acquisition, Formal analysis.

Declaration of competing interest

The authors declare that they have no known competing financial interests or personal relationships that could have appeared to influence the work reported in this paper.

Acknowledgement

This work was supported by Chalmers Gender Initiative for Excellence (Genie).

Appendix A. Supplementary data

Supplementary data to this article can be found online at https://doi.org/10.1016/j.memsci.2025.124914.

Data availability

Data will be made available on request.

References

- [1] R. Zhao, P. Jin, J. Zhu, Y. Li, G. Li, A. Volodine, Y. Liu, J. Zheng, B. Van der Bruggen, Amino acid-based loose polyamide nanofiltration membrane with ultrahigh water permeance for efficient dye/salt separation, J. Membr. Sci. 673 (2023) 121477, https://doi.org/10.1016/j.memsci.2023.121477.
- [2] P. Liu, H. Xu, P. Jin, X. Zhu, J. Zheng, Y. Liu, J. Yang, D. Xu, H. Liang, DFT-Assisted machine learning for polyester membrane design in textile wastewater recovery applications, Water Res. 279 (2025) 123438, https://doi.org/10.1016/j. watres.2025.123438.
- [3] Y. Zhao, Y. Liao, G.S. Lai, Y. Yin, R. Wang, A tight polyethersulfone ultrafiltration membrane fabricated via polyion complex assisted phase inversion for dye desalination, J. Membr. Sci. 685 (2023) 121908, https://doi.org/10.1016/j. memsci.2023.121908.
- [4] S. Jabbarvand Behrouz, A. Khataee, V. Vatanpour, Y. Orooji, Surface bioengineering of Mo2Ga2C MAX phase to develop blended loose nanofiltration membranes for textile wastewater treatment, ACS Appl. Mater. Interfaces 16 (2024) 10508–10521, https://doi.org/10.1021/acsami.3e16951.
- [5] N. Xu, J. Xue, W. Xu, P.S. Goh, A. Fauzi Ismail, F. Wang, Y. Xue, Y. Liu, Y. Wei, Facile preparation of antifouling Ti3C2Tx MXene membrane intercalated with ultrathin α-Co(OH)2 LDH nanosheets for selective dye/salt separation, Desalination 603 (2025) 118676, https://doi.org/10.1016/j.desal.2025.118676.
- [6] K. Khoiruddin, I.G. Wenten, U.W.R. Siagian, Advancements in bipolar membrane electrodialysis techniques for carbon capture, Langmuir 40 (2024) 9362–9384, https://doi.org/10.1021/acs.langmuir.3c03873.
- [7] Y. Xue, J.W. Chew, Sustainable carbonaceous materials-based catalytic membranes for organic wastewater treatment: progress and prospects, Sep. Purif. Technol. (2024) 131119.
- [8] L. Teng, C. Yue, G. Zhang, Epoxied SiO2 nanoparticles and polyethyleneimine (PEI) coated polyvinylidene fluoride (PVDF) membrane for improved oil water separation, anti-fouling, dye and heavy metal ions removal capabilities, J. Colloid Interface Sci. 630 (2023) 416–429, https://doi.org/10.1016/j.jcis.2022.09.148.
- [9] P. Zhou, S. Zhang, Y. He, J. Wu, L. Zhou, X. Yin, S. Tian, S. Li, W. Chen, One-pot fabrication of SF-DA@PVDF membrane for dye adsorption and oil-in-water emulsion separation, J. Environ. Chem. Eng. 11 (2023) 109730, https://doi.org/ 10.1016/j.jece.2023.109730.
- [10] L. Ren, R. Deng, J. Yang, J. Li, J. Jin, T. Lei, Improved hydrophilicity and antifouling performances of PVDF ultrafiltration membrane via in situ crosslinking, J. Mater. Sci. 58 (2023) 13854–13864, https://doi.org/10.1007/s10853-023_08870_5
- [11] Z. Wang, G. Feng, Z. Yan, S. Li, M. Xu, C. Wang, Y. Li, Improving the hydrophilicity and antifouling performance of PVDF membranes via PEI amination and further poly (methyl vinyl ether-alt-maleic anhydride) modification, React. Funct. Polym. 189 (2023) 105610, https://doi.org/10.1016/j.reactfunctpolym.2023.105610.
- [12] Z. Wu, X. Ji, Q. He, H. Gu, W. Zhang, Z. Deng, Nanocelluloses fine-tuned polyvinylidene fluoride (PVDF) membrane for enhanced separation and antifouling, Carbohydr. Polym. 323 (2024) 121383, https://doi.org/10.1016/j. carbool.2023.121383.
- [13] R. Pishbin, T. Mohammadi, M.A. Tofighy, PVDF ultrafiltration membranes containing copper oxide-charcoal based graphene oxide nanohybrids with enhanced performance and antifouling properties, Process Saf. Environ. Prot. 176 (2023) 180–195, https://doi.org/10.1016/j.psep.2023.05.086.
- [14] B. Li, Z. Yang, Y. Dou, J. Zhang, J. Lu, J. Han, Two-dimensional LDH film templating for controlled preparation and performance enhancement of polyamide nanofiltration membranes, Angew. Chem. Int. Ed. 62 (2023) e202304442, https:// doi.org/10.1002/anie.202304442.
- [15] Z. Cheng, J. Yang, L. Li, Y. Chen, X. Wang, Flocculation inspired combination of layered double hydroxides and fulvic acid to form a novel composite adsorbent for the simultaneous adsorption of anionic dye and heavy metals, J. Colloid Interface Sci. 618 (2022) 386–398, https://doi.org/10.1016/j.jcis.2022.03.097.
- [16] X. Du, S.A. Rashid, L.C. Abdullah, N.A. Rahman, Preparation of electrospun cellulose acetate/chitosan membranes for efficient sorption of heavy metals from aqueous solutions, Colloids Surf. A Physicochem. Eng. Asp. 699 (2024) 134698, https://doi.org/10.1016/j.colsurfa.2024.134698.
- [17] X. Lin, L. Chen, C. Chen, J. Rao, J. Chen, Y. He, Carboxylated-covalent organic frameworks and chitosan assembled membranes for precise and efficient dye separation, J. Membr. Sci. 663 (2022) 121075, https://doi.org/10.1016/j. memsci.2022.121075.
- [18] T. Li, R. Liu, S. Liu, J. Xu, J. Yu, L. Guo, F. Li, Highly permeable hybrid membranes constructed from MXene and TA-APTES nanoaggregates for effective dye/salt fractionation, J. Membr. Sci. 734 (2025) 124470, https://doi.org/10.1016/j. memsci.2025.124470.
- [19] Z. Yang, S. Li, X. Xia, Y. Liu, Hexagonal MgAl-LDH simultaneously facilitated active facet exposure and holes storage over ZnIn2S4/MgAl-LDH heterojunction for boosting photocatalytic activities and anti-photocorrosion, Sep. Purif. Technol. 300 (2022) 121819, https://doi.org/10.1016/j.seppur.2022.121819.
- [20] C. Huang, Y. Yang, P. Wang, H. Fu, X. Hu, Y. Zhou, L. Zhang, Y. Zhong, Synergistic acid-base action leads to ultrafast decontamination of nerve and blister agents by OH– intercalated Zr4+-Doped MgAl-LDH under ambient conditions, Adv. Mater. 37 (2025) 2412688, https://doi.org/10.1002/adma.202412688.

- [21] R. Zheng, W.-L. Zhao, H. Li, H. Hu, T. Lin, W. Chen, Y.-F. Song, Pyrazole-3,5-dicarboxylic acid intercalated LDH: a highly selective structured adsorbents for Cu2+ ions removal, Sep. Purif. Technol. 346 (2024) 127532, https://doi.org/10.1016/j.seppur.2024.127532.
- [22] R. Pourfaraj, S.J. Fatemi, S.Y. Kazemi, P. Biparva, Synthesis of hexagonal mesoporous MgAl LDH nanoplatelets adsorbent for the effective adsorption of brilliant yellow, J. Colloid Interface Sci. 508 (2017) 65–74, https://doi.org/ 10.1016/j.jcis.2017.07.101.
- [23] W. Mo, C. Wei, C. He, Y. Yang, M.N.L. Islahah, X. Su, J. Yang, Y. Huang, J. Feng, S. Ma, Fe304@Mg/Al/Fe-LDH adsorption properties of As(V) and As(III) coexisting in water, J. Water Proc. Eng. 68 (2024) 106444, https://doi.org/10.1016/ i.iwpe.2024.106444.
- [24] N. Xu, X. Wen, D.-D. Shi, X. Liu, J. Liu, K.-P. Zhong, Q. Gao, Q. Zhao, X. Han, S.-J. Bian, Facile synthesis of sodium dodecyl sulfate intercalated Mg-Al LDH and its excellent adsorption performances for Cu2+ from aqueous solution, ChemistrySelect 9 (2024) e202305210, https://doi.org/10.1002/slct.202305210.
- [25] M. khorshidi, S. Asadpour, N. Sarmast, Z. Aramesh-Boroujeni, N. Sadegh, Enhanced adsorption performance of tetracycline in aqueous solutions using Mg-Al-LDH/AC nanocomposite, Arab. J. Chem. 16 (2023) 105301, https://doi.org/ 10.1016/j.arabjc.2023.105301.
- [26] B. Lei, W. Cui, P. Chen, R. Chen, Y. Sun, K.-H. Kim, F. Dong, Rational design of LDH/Zn2SnO4 heterostructures for efficient mineralization of toluene through boosted interfacial charge separation, ENERGY & ENVIRONMENTAL MATERIALS 6 (2023) e12291, https://doi.org/10.1002/eem2.12291.
- [27] H. Yang, H. Hou, M. Yang, Z. Zhu, H. Fu, D. Zhang, Y. Luo, W. Yang, Engineering the S-scheme heterojunction between NiO microrods and MgAl-LDH nanoplates for efficient and selective photoreduction of CO2 to CH4, Chem. Eng. J. 474 (2023) 145813, https://doi.org/10.1016/j.cej.2023.145813.
- [28] W. Wang, X. Shen, Y. Liu, M. Han, Y. Zhai, A novel fluoride removal adsorbent of a Zr4+-Doped Mg-al-layered double hydroxide: synthesis and fluoride removal performance, Ind. Eng. Chem. Res. 64 (2025) 5949–5961, https://doi.org/ 10.1021/acs.iecr.4c04979.
- [29] Q. Bai, X. Wang, Y. Zhang, Y. Wang, C. Li, Y. Wang, X. He, Y. Shen, H. Uyama, Dual-channels engineering of carbon tube/NiCo-LDH composites for enhanced ion diffusion and electron transfer, Chem. Eng. J. 512 (2025) 162094, https://doi.org/ 10.1016/j.cej.2025.162094.
- [30] J. Wang, Y. Liang, Z. Wang, B. Huo, C. Liu, X. Chen, H. Xu, D. Li, Z. Zhu, Y. Wang, F. Meng, High efficiently degradation of organic pollutants via low-speed water flow activation of Cu2O@MoS2/PVDF modified pipeline with biocatalysis performance, Chem. Eng. J. 458 (2023) 141409, https://doi.org/10.1016/j.cei.2023.141409.
- [31] E.S. Kadir, R.N. Gayen, Improved UV sensitivity in solution-processed PVDF/ZnO nanocomposites via piezo-phototropic effect, Mater. Today Commun. 39 (2024) 109174, https://doi.org/10.1016/j.mtcomm.2024.109174.
- [32] T.S. Soliman, Exploring the potential of Pr6O11 nanoparticles in enhancing PVDF phases and optical parameters, Inorg. Chem. Commun. 176 (2025) 114235, https://doi.org/10.1016/j.inoche.2025.114235.
- [33] J. Gao, X. Tang, Y. Chen, Y. Liu, Shape-stabilized phase change material with enhanced thermal conductivity fabricated based on biomimetic polymerization and in situ reduction of Cu ions, Int. J. Energy Res. 45 (2021) 2058–2069, https:// doi.org/10.1002/er.5898.
- [34] G. Zhu, M. Zou, W. Luo, Y. Huang, W. Chen, X. Hu, X. Jiang, Q. Li, A polyurethane solid-solid phase change material for flexible use in thermal management, Chem. Eng. J. 488 (2024) 150930, https://doi.org/10.1016/j.cej.2024.150930.
- [35] A.H. Bashal, K.D. Khalil, A.M. Abu-Dief, M.A. El-Atawy, Cobalt oxide-chitosan based nanocomposites: synthesis, characterization and their potential pharmaceutical applications, Int. J. Biol. Macromol. 253 (2023) 126856, https://doi.org/10.1016/j.ijbiomac.2023.126856.
- [36] A.M. Shehap, R.A. Nasr, M.A. Mahfouz, A.M. Ismail, Preparation and characterizations of high doping chitosan/MMT nanocomposites films for removing iron from ground water, J. Environ. Chem. Eng. 9 (2021) 104700, https://doi.org/10.1016/j.jece.2020.104700.
- [37] X. Han, Y. Mi, Y. Ji, M. Sun, H. Tang, F. Dong, Z. Guo, A novel chitosan antioxidant bearing sulfhydryl group: synthesis, characterization and activity assessment, Int. J. Biol. Macromol. 261 (2024) 129816, https://doi.org/10.1016/j. ijbiomac.2024.129816.
- [38] S. Zhang, F. Dai, Q. Wang, G. Qian, C. Chen, Y. Yu, The fabrication of porous hollow polysulfone microspheres with PEG as a porogen for methylene blue adsorption, Colloids Surf. A Physicochem. Eng. Asp. 634 (2022) 127949, https:// doi.org/10.1016/j.colsurfa.2021.127949.
- [39] L. Zou, X. Zhang, P. Gusnawan, G. Zhang, J. Yu, Crosslinked PVDF based hydrophilic-hydrophobic dual-layer hollow fiber membranes for direct contact membrane distillation desalination: from the seawater to oilfield produced water, J. Membr. Sci. 619 (2021) 118802, https://doi.org/10.1016/j. memsci.2020.118802.
- [40] T. Liu, S. Gou, Y. He, S. Fang, L. Zhou, G. Gou, L. Liu, N-methylene phosphonic chitosan aerogels for efficient capture of Cu2+ and Pb2+ from aqueous environment, Carbohydr. Polym. 269 (2021) 118355, https://doi.org/10.1016/j. carbpol.2021.118355.
- [41] X. Su, X. Wang, Z. Ge, Z. Bao, L. Lin, Y. Chen, W. Dai, Y. Sun, H. Yuan, W. Yang, J. Meng, H. Wang, S.C. Pillai, KOH-Activated biochar and chitosan composites for efficient adsorption of industrial dye pollutants, Chem. Eng. J. 486 (2024) 150387, https://doi.org/10.1016/j.cej.2024.150387.
- [42] R. Chen, B. Cai, R. Liu, W. Xu, X. Jin, L. Yu, Q. Wang, Q. Yong, Synergistic and antagonistic adsorption mechanisms of copper(II) and cefazolin onto bio-based chitosan/humic composite: a combined experimental and theoretical study,

- J. Environ. Chem. Eng. 12 (2024) 113061, https://doi.org/10.1016/j.jece.2024.113061.
- [43] T. Thayyullathil, T. Francis, A. Stephy, A. Padmanabhan, Thermal degradation kinetics studies of polyvinylidene fluoride/ZSM-5 hybrid nanofiber by thermogravimetric analysis, Thermal Advances 3 (2025) 100035, https://doi.org/ 10.1016/j.thradv.2025.100035.
- [44] J. Zhu, B. Zeng, L. Mo, F. Jin, M. Deng, Q. Zhang, One-pot synthesis of MgAl layered double hydroxide (LDH) using MgO and metakaolin (MK) as precursors, Appl. Clay Sci. 206 (2021) 106070, https://doi.org/10.1016/j.clay.2021.106070.
- [45] N. Hsan, P.K. Dutta, S. Kumar, J. Koh, Arginine containing chitosan-graphene oxide aerogels for highly efficient carbon capture and fixation, J. CO2 Util. 59 (2022) 101958, https://doi.org/10.1016/j.jcou.2022.101958.
- [46] H. Zeng, Z. Yu, L. Shao, X. Li, M. Zhu, Y. Liu, X. Feng, X. Zhu, A novel strategy for enhancing the performance of membranes for dyes separation: embedding PAA@ UiO-66-NH2 between graphene oxide sheets, Chem. Eng. J. 403 (2021) 126281, https://doi.org/10.1016/j.cej.2020.126281.
- [47] N.K. Hundessa, C.-C. Hu, D.-Y. Kang, P.-C. Chou, E.G. Ajebe, K.-R. Lee, J.-Y. Lai, Ultra-high flux loose nanofiltration membrane based on metal organic framework (CAU-10-H)/P84 co-polyimide for dye/salt fractionation from industrial waste water, Desalination 586 (2024) 117871, https://doi.org/10.1016/j. desal 2024 117871
- [48] Q. Ye, J. Li, Y. Huang, H. Wu, Y. Li, B. Yan, Preparation of a Cyclodextrin metalorganic framework (CD-MOF) membrane for chiral separation, J. Environ. Chem. Eng. 11 (2023) 109250, https://doi.org/10.1016/j.jece.2022.109250.
- [49] J. Farahbakhsh, M. Golgoli, M. Najafi, S.Z. Haeri, M. Khiadani, A. Razmjou, M. Zargar, An innovative NH2-UiO-66/NH2-MIL-125 MOF-on-MOF structure to improve the performance and antifouling properties of ultrafiltration membranes, Sep. Purif. Technol. 353 (2025) 128273, https://doi.org/10.1016/j.seppur.2024.128273.
- [50] A. Abdel-Karim, S. Leaper, M. Alberto, A. Vijayaraghavan, X. Fan, S.M. Holmes, E. R. Souaya, M.I. Badawy, P. Gorgojo, High flux and fouling resistant flat sheet polyethersulfone membranes incorporated with graphene oxide for ultrafiltration

- applications, Chem. Eng. J. 334 (2018) 789–799, https://doi.org/10.1016/j.cei.2017.10.069.
- [51] X. Wang, R. Rehman, K. Zhang, K. Fan, A. Hu, Z. Zhang, Y. Liu, S. Xia, D. Yin, P. Li, Enhancement separation selectivity of mineral ions and perfluorinated and polyfluoroalkyl substances by nanofiltration membrane through hydrogel-assisted interfacial polymerization, Water Res. 280 (2025) 123498, https://doi.org/ 10.1016/j.watres.2025.123498.
- [52] C. Yu, Y. He, Y. Zhang, Y. Deng, Y. Qi, Q. Liu, Y. Liang, Superfast water transport mixed matrix membranes with asymmetrical micro-nanostructures reinforced by metal-organic frameworks, Water Res. 282 (2025) 123767, https://doi.org/ 10.1016/j.watres.2025.123767.
- [53] Z. Li, Y. Liu, X. Wei, Z. Zhang, F. Zhao, T. Wang, Y. Du, E. Shi, C. Fan, Y. Yang, Z. Jiang, Antifouling polyvinylidene fluoride membrane through dopamine self-polymerization enhanced surface segregation toward oil-in-water emulsions separation, Adv. Funct. Mater. 34 (2024) 2405915, https://doi.org/10.1002/adfm.202405915.
- [54] X. Zhuang, S.W. Han, M.C. Shin, J.Y. Hwang, J.H. Park, Optimized antifouling γ-Al2O3/α-Al2O3 nanofiltration composite membrane for lignin recovery from wastewater, Water Res. 267 (2024) 122418, https://doi.org/10.1016/j. wastewater 2024 122418
- [55] X. Yang, X. Chen, X. Su, A. Cavaco-Paulo, H. Wang, J. Su, A backbone support structure and capillary effect-induced high-flux MOF-based mixed-matrix membrane for selective dye/salt separation, Sep. Purif. Technol. 344 (2024) 127221, https://doi.org/10.1016/j.seppur.2024.127221.
- [56] J. Han, J. Li, X. Zhang, L. Zhao, C. Wang, Enhancing the performance of triboelectric nanogenerator via chitosan films surface modification, Chem. Eng. J. 489 (2024) 151493, https://doi.org/10.1016/j.cej.2024.151493.
- [57] Y. Yuan, W. Tan, J. Zhang, Q. Li, Z. Guo, Water-soluble amino functionalized chitosan: preparation, characterization, antioxidant and antibacterial activities, Int. J. Biol. Macromol. 217 (2022) 969–978, https://doi.org/10.1016/j. ijbiomac.2022.07.187.